

# Mutual Synchronization for Power Generation and Beam-Steering in CMOS With On-Chip Sense Antennas Near 200 GHz

Kaushik Sengupta, *Member, IEEE*, and Ali Hajimiri, *Fellow, IEEE*

**Abstract**—In this paper, we introduce the concept of near-field synchronization as an efficient, scalable, and robust method to synchronize a 2-D array of mutually coupled oscillators for beam-forming at frequencies above  $f_{\max}$  of a technology. The method employs an array of on-chip sense antennas to probe electromagnetic near-fields of the on-chip radiators. These sense antennas are then coupled to each other appropriately through a network that establishes the synchronized state as the lowest energy state. A circuit-electromagnetic co-design methodology is employed to demonstrate beam-steering near 200 GHz with a synchronized  $2 \times 2$  array. Each element of the array is a traveling-wave oscillator with the nonlinear active devices selectively radiating its second harmonic through the same electromagnetic structure. The beam-pattern can be varied by more than  $70^\circ$  in both azimuth and elevation. The chip is realized in 65-nm bulk CMOS.

**Index Terms**—Beam-forming, beam-steering, CMOS, millimeter wave, near-field, terahertz, on-chip antenna, power combining, power generation, substrate modes.

## I. INTRODUCTION

HIGHER millimeter-wave and terahertz frequencies have various desirable properties, which can impact an array of diverse fields such as communication, security, healthcare, sensing, global environment monitoring, and industrial safety [1]–[3]. High-frequency Gunn and IMPATT diodes have been used to generate power in the milliwatt range in this frequency band [4]–[6]. Further, single chip solutions with III–V-based monolithic microwave integrated circuits (MMICs) have been demonstrated at 300 GHz [5]. In recent years, silicon-based circuit technology has emerged as a low-cost alternative demonstrating fully integrated systems [7]–[10]. However, enabling an efficiently radiating terahertz source in CMOS has been very challenging [11], [12]. In addition to limited  $f_{\max}$  and low breakdown voltages of CMOS devices, extracting the generated power out of the lossy substrate using integrated

antennas with low surface waves is a non-trivial problem [13], [14].

One way to overcome the limitations of power generation of a single device and suppress surface waves simultaneously is to deploy multiple synchronized power (say,  $N$ ) sources in a suitably arranged array configuration [13]. This enables quasi-optical power combining ( $\times N$ ), increased effective-isotropic-radiative power (EIRP) ( $\times N^2$ ), and potentially electronic beam-steering by incorporating individual phase control in each of the radiating elements.

Multiple techniques to synchronize arrays of mutually coupled oscillators, such as nearest neighbor coupling through transmission lines (t-lines) and spurious radiation, were proposed and demonstrated at microwave frequencies mostly in discrete designs [15]–[22]. In [15]–[18], arrays of mutually coupled oscillators were realized to combine power coherently in free space. In [21] and [22], a periodic oscillator array mounted in an open quasi-optical cavity was employed to emulate an active gain medium, such as in a laser. In recent years, integrated arrays, synchronized either through mutual coupling or locked to a central frequency reference, have been demonstrated to combine power on-chip and quasi-optically in the 200–400-GHz range to produce broadside radiation patterns [26]–[29], [32]. Further, electronic beam-scanning was demonstrated in [30] and [33], by locking multiple elements to a central frequency reference through sub-harmonic locking. In this paper, we propose a scalable methodology to mutually lock a 2-D array of oscillating and radiating power sources by sensing their near-electromagnetic fields to enable beam-forming and beam-steering at frequencies near and above  $f_{\max}$  of a technology.

This paper is organized as follows. Section II describes the detailed electromagnetic theory behind the concept. Section III presents an analysis of locking bandwidth, beam-scanning range, and stability. The design and measurement results are presented in Section IV.

## II. NEAR-FIELD SENSING AND ON-CHIP SYNCHRONIZATION OF LARGE-SCALE ARRAYS

Consider an array of  $N$  self-sustained and radiating oscillators, which are mutually coupled to their nearest neighbors for synchronization, as shown in Fig. 1. The key idea behind synchronization is to establish the desired locked condition as the lowest energy state and the only stable steady state. This ensures that when the oscillators start up, the coupling network

Manuscript received September 19, 2014; revised February 20, 2015; accepted July 06, 2015. Date of publication July 31, 2015; date of current version September 01, 2015.

K. Sengupta was with the Department of Electrical Engineering, California Institute of Technology, Pasadena, CA 91125 USA. He is now with the Department of Electrical Engineering, Princeton University, Princeton, NJ 08544 USA (e-mail:kaushiks@princeton.edu).

A. Hajimiri is with the Department of Electrical Engineering, California Institute of Technology, Pasadena, CA 91125 USA (e-mail:hajimiri@caltech.edu).

Color versions of one or more of the figures in this paper are available online at <http://ieeexplore.ieee.org>.

Digital Object Identifier 10.1109/TMTT.2015.2457902

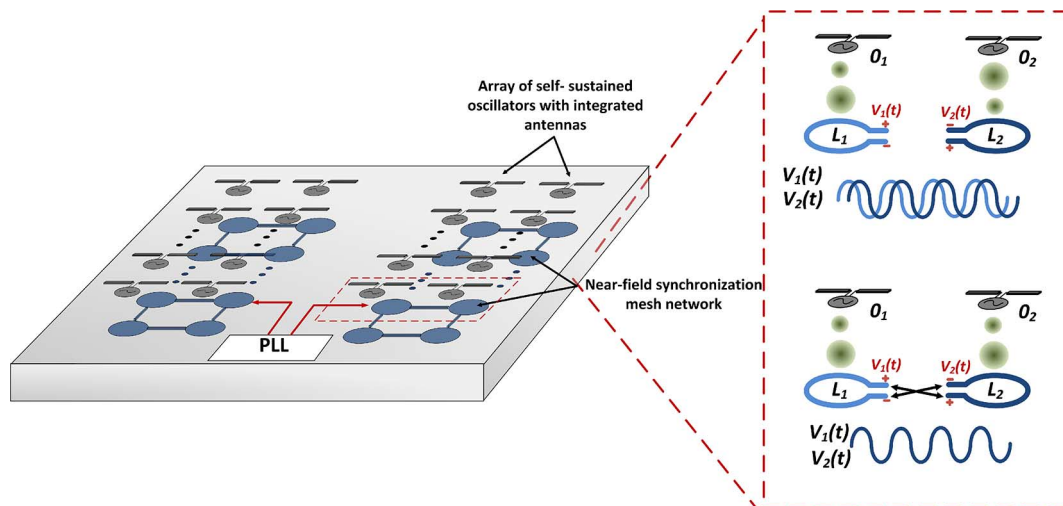


Fig. 1. Near-field synchronization architecture: sets of self-sustained oscillator-cum radiator elements are synchronized by an underlying network of near-field sensors. The distributed electromagnetic approach enables optimized design and placement of the array elements without the constraints of traditional t-line-based networks.

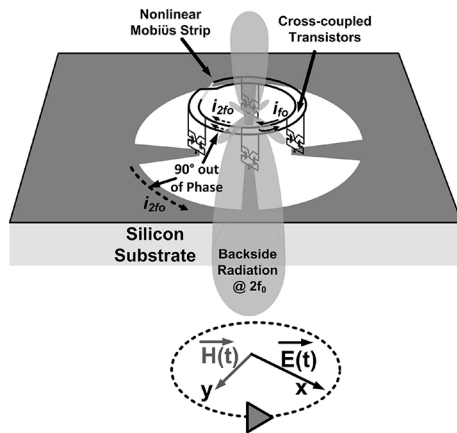


Fig. 2. DAR: traveling-wave oscillator at  $f_0$  combined with frequency doubling and selective radiation of the second harmonic signal  $2f_0$  in a circularly polarized fashion.

sustains transient currents, which inject currents back into the one or more of the coupled oscillators, pulling them into the synchronized mode. If the signal at a harmonic frequency needs to be extracted from the array to generate power beyond  $f_{\max}$ , then the locking network should not load the synchronized oscillators either at the fundamental or at any of the desired harmonic frequencies.

Near-field locking exploits the fact that the information of phase and frequency of each array element is not just contained in the dynamics of voltage or current, but also in the electromagnetic near-fields. The conceptual idea is illustrated in Fig. 1. Let there be two uncoupled free-running oscillators  $O_1$  and  $O_2$  radiating out of the shared substrate. The individual radiated fields are sensed by two identically placed “sense” antennas  $L_1$  and  $L_2$  with respect to the sources  $O_1$  and  $O_2$ , respectively. Without any locking mechanism,  $O_1$  and  $O_2$  will oscillate at similar frequencies, but at random phases, which is reflected at the sense antenna terminal voltages  $V_1(t)$  and  $V_2(t)$ , as shown in Fig. 1. *If the sense antennas are now coupled appropriately so that the most stable steady-state condition is when the terminal voltages  $V_1(t)$  and  $V_2(t)$  equalize, then it will also force equalization of*

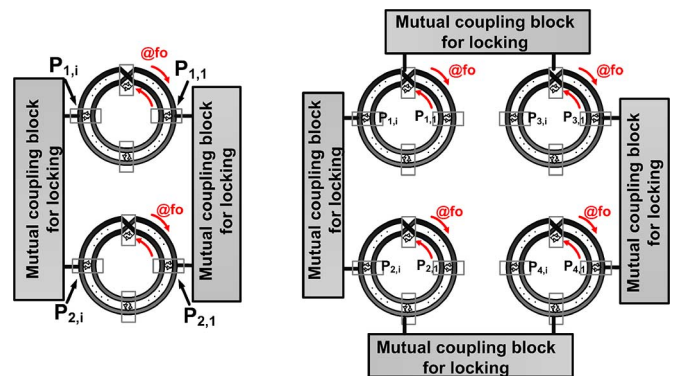


Fig. 3. Limitations in scalability of t-line-based coupling networks required for coherent synchronization.

*the individual near-fields and synchronization of the source oscillators.* Thereby, the free-running oscillators  $O_1$  and  $O_2$  can be “wirelessly” locked (Fig. 1). This method of coupling through radiated fields allows us to decouple the design, optimization, and placement of each array element from the coupling network. Further, unlike direct sensing of voltages and currents, this distributed electromagnetic-circuit approach to sensing the near-fields can result in very different and desirable behaviors at the fundamental and the harmonic frequencies, as explained in the following sections. The operation principle of the proposed method will be discussed with traveling-wave oscillators as the individual array element. However, the proposed concept of near-field synchronization is general and is applicable to arrays of any form of free-running autonomous radiating sources.

#### A. T-Line Coupling for Array Synchronization

In this section, we will highlight the limitations of scalability of nearest neighbor coupling using t-lines. This will be discussed in the context of locking an array of radiating frequency-doubling traveling-wave oscillators, which we refer to as the distributed active radiators (DARs) [33]. As shown in Fig. 2, the DAR converts dc power into a radiated signal above  $f_{\max}$ . The structure consists of two loops with multiple differential

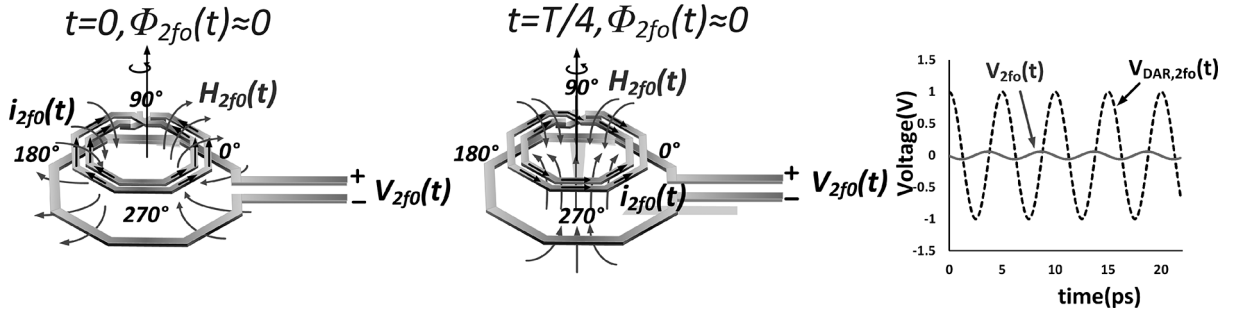


Fig. 4. In-phase traveling-wave second harmonic currents rotate about the broadside axis with time, leading to almost zero magnetic flux through the sense antenna aperture. The sense antenna, therefore, is effectively transparent to the second harmonic radiation.

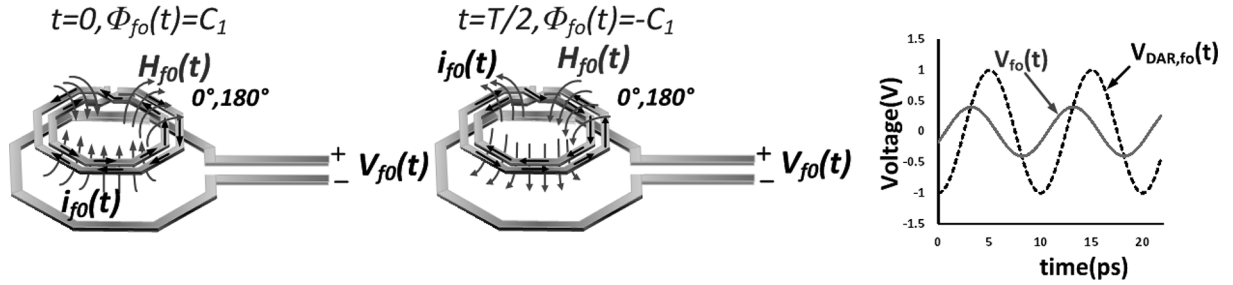


Fig. 5. Out-of-phase fundamental frequency currents in the two branches do not cancel their fields in the near-field region, leading to a periodically changing flux at the fundamental frequency. The sense antenna, therefore, primarily picks up the signal at the fundamental frequency.

cross-coupled transistors that sustain a traveling-wave oscillation at a fundamental frequency  $f_0$  where the loop phase is  $180^\circ$ . As can be seen in Fig. 2, the currents at  $f_0$  are out-of-phase, which quasi-optically suppresses radiation at the fundamental frequency. However, the second-harmonic currents above  $f_{\max}$ , generated by transistor nonlinearities, flow in phase and radiate out selectively through the aperture and the substrate (Fig. 2). It can be noted that both the fundamental and second harmonic signals on the loops are traveling waves. Therefore, the radiated electromagnetic fields in space ( $\vec{E}$  and  $\vec{H}$ ) are circularly polarized and rotates about the vertical axis with time (Fig. 2).

If two of these traveling-wave oscillators need to be synchronized for quasi-optical power combination, then all the corresponding cross-coupled pairs should oscillate in phase. As shown in Fig. 3, this can be achieved using two judiciously placed t-line-based networks [25]. For larger arrays, a set of  $2 \times 1$  arrays can be used as a single element and the same principle may be used in an iterative way, as shown in Fig. 3.

Evidently, scaling to large 2-D arrays using such complex interconnected network of t-lines becomes prohibitively difficult. In order to accommodate such networks, the radiator cores are often sub-optimally placed, which can lead to poor radiation pattern and lower efficiency due to the inability to suppress substrate modes [13]. Synchronizing with distributed electromagnetic-field sensors allows us to decouple these multiple constraints.

### B. On-Chip Near-Field Sensing

Figs. 4 and 5 show the layout of the DAR radiator core and the sense antenna located in its near-field region. Since the sense antenna can pick up the different harmonic frequencies, it is important to understand how its presence can affect the near- and

far-field radiation patterns, and how different harmonics contribute to the locking mechanism. As explained in Section II-A, the DARs predominantly radiate the  $2f_0$  component and radiation at the fundamental frequency ( $f_0$ ) is mostly suppressed by the out-of-phase currents in the two concentric loops. However, the sense antenna primarily picks up the near-fields at  $f_0$ , while almost not affecting the desired  $2f_0$  radiation patterns.

This is explained in Figs. 4 and 5. The second-harmonic voltage  $V_{2f_0}(t)$  at the terminal of the sense antenna is related to the rate of change of magnetic flux  $\Phi_{2f_0}(t)$  generated by the traveling-wave structure and coupled to the sense antenna. Therefore,  $V_{2f_0}(t) = (d\Phi_{2f_0}(t))/(dt)$ .

As illustrated in Fig. 4,  $2f_0$  currents form in-phase traveling waves over the concentric loops of the DAR, which are one wavelength long. Therefore, with time, the  $2f_0$  current configuration and the associated magnetic fields essentially rotate about the broadside axis, as shown in Fig. 4. Hence, by rotational symmetry, the  $2f_0$  magnetic flux linkage to the sense antenna remains almost constant (almost zero) with time. Therefore, we have

$$\Phi_{2f_0}(t) \approx 0 \quad (1a)$$

$$V_{2f_0}(t) \approx 0. \quad (1b)$$

As a result, the voltage picked up at the sense antenna terminal ( $V_{2f_0}(t)$ ) is negligible, even when a second harmonic traveling wave of amplitude 1 V exists on the traveling-wave loops at  $2f_0 = 200$  GHz.<sup>1</sup> Of course, the presence of the sense antenna leads to local scattering of the near-fields, which can lead to

<sup>1</sup>In reality, the  $2f_0$  wave amplitude on the DAR will be much less than 1 V, and therefore, the sense antenna  $2f_0$  voltage will be even less. The structure is simulated in Ansys HFSS, a 3-D electromagnetic simulation tool that uses the finite-element method.

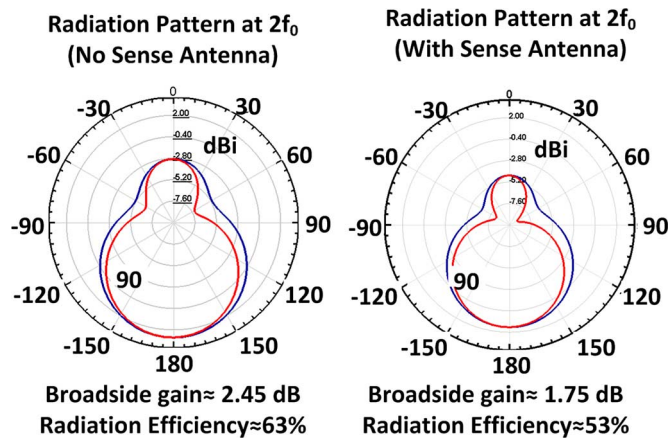


Fig. 6. Second harmonic radiation pattern of a single traveling-wave radiating structure in the presence and absence of the sense antenna. The sense antenna is terminated with the boundary conditions of a synchronized state.

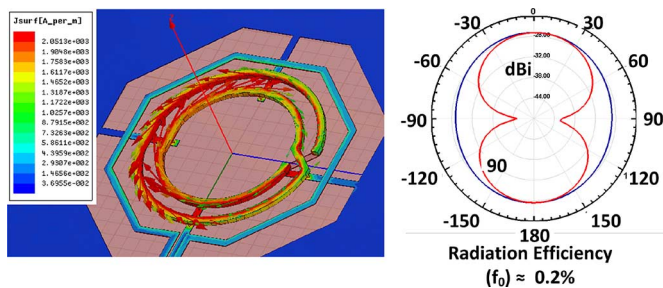


Fig. 7. Impressed current at fundamental frequency ( $f_0$ ) on the sense antenna at steady state is much smaller compared to the fundamental signal on the traveling-wave oscillator loops. The far-field cancellation is still effective at  $f_0$  with only 0.2% radiation efficiency and  $-26$ -dB radiation gain. The simulations were performed in the 3-D finite-element electromagnetic simulator Ansys HFSS.

a small, but observable  $V_{2f_0}(t)$  at the sense antenna terminal (Fig. 4) due to its own self-inductance. Therefore, the oscillator and sense-antenna pair needs to be co-optimized to reduce the second harmonic pick-up. The small  $2f_0$  current impressed on the sense antenna can, however, lead to ohmic loss. The radiation efficiency of a single DAR reduces from 63% to 53% and the corresponding gain from 2.45 to 1.75 dB, as shown in Fig. 6. However, as shown in the same figure, the radiation pattern of a single radiating element is almost unchanged in the presence of the sense antenna under the locked condition.

The current distribution at the fundamental frequency ( $f_0$ ) in a DAR does not possess the rotational symmetry of its second harmonic. As is evident from Fig. 5, the out-of-phase currents in the two branches cancel their radiation only in the far-field. In the near-field region, the strength of the magnetic fields contributed by the two branches are significantly different. This results in a periodically changing magnetic flux ( $\Phi_{f_0}$ ) at  $f_0 = 100$  GHz through the sense antenna aperture, and consequently, a significant pick-up is registered at the sense antenna terminal (Fig. 5). Further, the presence of the sense antenna does not significantly affect the far-field cancellation of the  $f_0$  signal. As illustrated in the electromagnetic simulation results in Fig. 7, the DAR remains a very inefficient radiator at  $f_0$  in the presence of the sense antenna with an efficiency of 0.2%.

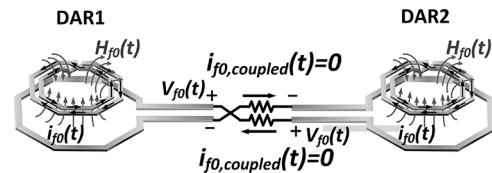


Fig. 8. Coupling network between the sense antenna terminals to synchronize neighboring DARs. The network ensures that no power is dissipated when the sources are synchronized, making it the lowest energy state.

It should be noted that near-field synchronization is inherently different from a lumped transformer coupling network. The dimension of the sense antenna is comparable to the wavelength at the frequency of operation, resulting in very different behaviors at the fundamental and harmonic frequencies, unlike a lumped transformer. In summary, in this method of near-field sensing, the radiated harmonic pattern remains almost unaffected by the presence of the sense network, while a small fraction of the fundamental power is sensed during the transient phase of locking. Once the system is locked, very little power gets wasted in the coupling network.

### C. Near-Field Synchronization for Power Combining and Beam-Scanning

Fig. 8 shows the near-field coupling network to synchronize two neighboring DARs. It can be seen that in the synchronized state, the terminal voltages of the sense antennas equalize and no steady-state current flows through the resistors. Therefore, no power gets dissipated in the coupling network. This establishes the locked state as the lowest energy state. Any perturbation from this state causes transient currents injected back into the traveling-wave oscillators, pulling them into the mutually synchronized mode.

The locking range is maximized by appropriately choosing the resistor that maximizes power dissipation in the network if the corresponding oscillators were out of phase. Fig. 9 shows the optimal value for coupling the DARs implemented in this paper for simulated fundamental frequency of oscillation of  $f_0 = 110$  GHz.<sup>2</sup>

The near-field locking method can be scaled to large-scale 2-D arrays of coherent radiating sources. As shown in Fig. 10, for the  $2 \times 2$  array, two sets of synchronized  $2 \times 1$  arrays are locked together with another set of sense antennas and the method can be extended for larger arrays. Unlike the radiative coupling method with spurious fields in [19], the placement of the radiator cores is no longer constrained by the locking network. Therefore, the power sources, their placements, radiation patterns, and beam-scanning range can be independently optimized, while a background mesh of coupled sense antennas ensures synchronization.

By incorporating phase control on the radiated signal from each element, the array can achieve electronic beam-scanning

<sup>2</sup>It can be shown that there exists two current configurations on the two loops, with wave travel in opposite directions, which can result in the same sense antenna voltage. However, the false locking states in the above two cases are unstable. The details are discussed in Appendix A. In practical implementation in a silicon die, any form of residual coupling through the substrate or otherwise is enough to suppress this undesired locking state and this is verified in simulations and experiments.

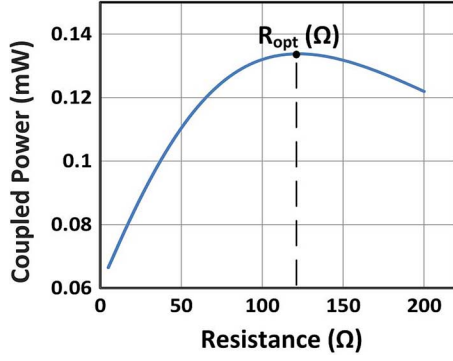


Fig. 9. Optimal value of coupling resistors to maximize locking range.

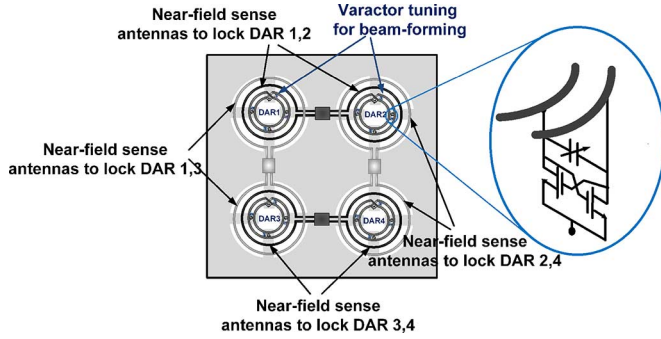


Fig. 10. Two sets of synchronized  $2 \times 1$  arrays locked together with two more sense antennas to form a  $2 \times 2$  array of traveling-wave radiators. The frequency tuning using varactor enables beam-steering through the synchronization network.

in 2-D space at frequencies above  $f_{\max}$ . The method to introduce phase control in an array of coupled oscillators by controlling the tuning frequency of the end elements was shown in [16]–[18]. We use a similar method, where we control the free-running oscillation frequency of each element in the array with varactors distributed along the resonator, as shown in Fig. 10. It should be noted that since the second harmonic is the dominant radiated signal, a phase difference of  $\phi$  at the fundamental frequency ( $f_0$ ) translates to a phase difference of  $2\phi$  at the radiated second harmonic frequency ( $2f_0$ ).

### III. LOCKING BANDWIDTH AND STEADY-STATE ANALYSIS

This section presents an analysis of the achievable locking and beam-scanning range. In a coupled system (Fig. 8), multiple cross-coupled pairs distributed in one DAR interacts with the other pairs in the neighboring DAR with different amplitudes and delays. Therefore, it is not possible to apply directly the arguments and results derived for a nearest neighbor coupling system in [16]–[18]. A general nonlinear dynamical description of such a multi-order system is also very complex. We will introduce arguments about rotational symmetry to simplify the analysis.

#### A. Analysis Approach: Dimension Reduction of Problem by Exploiting Symmetry

A negative- $g_m$  cell in a synchronized DAR is modeled as an oscillator with nonlinear transconductance ( $f(v) = \alpha_1 v -$

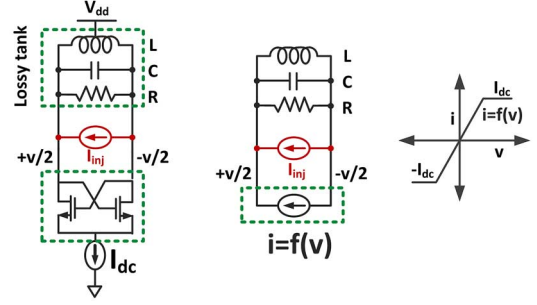


Fig. 11. Injection locking in a self-sustained oscillator and its nonlinear modeling.

$\alpha_3 v^3$ ) under injection  $i_{inj}(t)$ , as shown in Fig. 11. The system is governed by second-order dynamics due to the  $LC$  tank and by applying Kirchoff's current law (KCL) in Fig. 11, we can derive the state equations as

$$i_L + C \frac{dv}{dt} + i_R = f(v) + i_{inj} \quad (2)$$

$$\frac{1}{\omega_t^2} \frac{d^2 v}{dt^2} + \frac{1}{Q\omega_t} (1 - g_m R + 3\alpha_3 R v^2) \frac{dv}{dt} + v - L \frac{d i_{inj}}{dt} = 0 \quad (3)$$

where  $\omega_t = 1/\sqrt{LC}$  is the resonant frequency of the tank with quality factor  $Q = R/(\omega_t L)$ .

In general, the injected current  $i_{inj}$  into a transistor pair in a DAR is the result of the combined pulling effect of other cross-coupled pairs in the neighboring DAR with different delays. However, due to the rotational symmetry of the two structures, the delay between each corresponding pair in the two DARs is identical. This implies every cross-coupled pair will experience the same pulling current  $|i_{inj}|$  proportional to the difference between the voltages of the corresponding pair. Therefore, the entire dynamics of nonlinear synchronization is captured by analysis of any two corresponding cross-coupled pairs.

#### B. Steady-State Analysis: Beam-Scanning and Locking Range

Let  $v_1 = A \cos(\omega_0 t)$  and  $v_2 = A \cos(\omega_0 t + \phi)$  be the steady-state voltages of two corresponding cross-coupled pairs in two coupled DARs with slightly different resonance frequencies  $\omega_{t,1}$  and  $\omega_{t,2}$ . The injected current  $i_{inj}$  in the cross-coupled pair in DAR 1, as argued before, can be represented as  $i_{inj,1} = \varepsilon(v_2 - v_1) = \varepsilon A (\cos(\omega_0 t + \phi) - \cos(\omega_0 t))$ . Putting these values in (3) for the two DARs and simplifying, we obtain

$$\omega_0 = \frac{\sqrt{2}\omega_{t,1}\omega_{t,2}}{\sqrt{\omega_{t,1}^2 + \omega_{t,2}^2}} \quad (4)$$

$$\sin(\phi) = \frac{1}{\varepsilon L \omega_0} \frac{\omega_{t,2}^2 - \omega_{t,1}^2}{\omega_{t,1}^2 + \omega_{t,2}^2} \approx \frac{\Delta\omega_t}{C\omega_0} \quad (5)$$

where  $\Delta\omega_t = \omega_{t,2} - \omega_{t,1}$  and  $C \approx \varepsilon L \omega_0$  denotes the coupling strength. As expected, the induced phase difference  $\phi$  decreases for higher coupling strength  $C$ . Since  $|\sin(\phi)| \leq 1$ , the locking bandwidth can be expressed as

$$\Delta\omega_{\text{locking}} = C\omega_0. \quad (6)$$

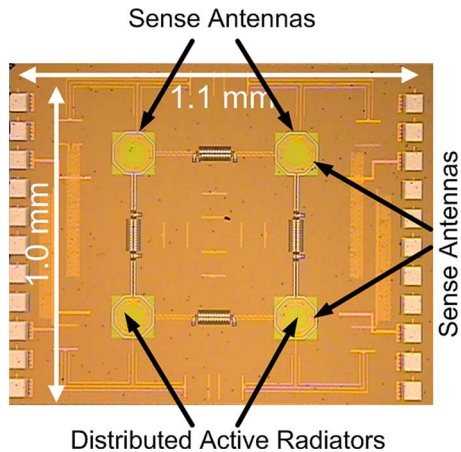


Fig. 12. Die photograph of the  $2 \times 2$  array.

It can be seen that the locking bandwidth is independent of the quality factors of the two resonators as long as the oscillators are operating in the current-limited regime. This is simply due to the fact that locking bandwidth  $\Delta\omega_{\text{locking}} = (i_{\text{inj}}\omega_0)/(2i_{\text{osc}}Q)$  varies inversely as  $Q$  and the injection current  $i_{\text{inj}} = \varepsilon(v_2 - v_1)$  also increases proportionately with  $Q$  in the current-limited region. For the DAR implemented in this paper, the simulated injected current when the coupled DARs are completely out of phase is  $i_{\text{inj}} \approx 750 \mu\text{A}$ . Under this condition,  $|v_2 - v_1| \approx 1 \text{ V}$  implying  $\varepsilon \approx 750 \mu\text{S}$ . The simulated resonator parameters are  $L\omega_0 \approx 50 \Omega$  and  $Q \approx 6$ , which results in the coupling coefficient to be  $C \approx 3.5\%$ . The locking bandwidth from (6) is then estimated to be approximately 4 GHz for a fundamental frequency of 110 GHz. The analysis of the stability of the synchronized state is presented in the Appendices A and B.

#### IV. DESIGN, IMPLEMENTATION, AND MEASUREMENT RESULTS

A  $2 \times 2$  array of mutually coupled DARs with a near-field synchronization network is designed in a 65-nm bulk CMOS process with  $f_{\text{max}} \sim 160 \text{ GHz}$ . The fundamental frequency of oscillation  $f_0$  is chosen to be 110 GHz, which implies that the desired radiated signal is at  $2f_0 = 220 \text{ GHz}$ . Each cross-coupled pair consists of NMOS transistors of  $W/L = 12 \mu\text{m}/65 \text{ nm}$  biased at 6 mA under 0.8 V. The resonator/antenna is realized on a  $3.2\text{-}\mu\text{m}$ -thick top copper metal layer with four cross-coupled pairs distributed along the circumference to sustain the traveling-wave oscillation at  $f_0 = 110 \text{ GHz}$  [37].<sup>3</sup> The sense antennas, as shown in Fig. 10, are realized on an upper and lower metal layer. The ground aperture is designed to have a radius of  $95 \mu\text{m}$  for the maximum second harmonic power generation and radiation [33]. The die photograph is shown in Fig. 12. Near-field sense and coupling networks are used for mutual synchronization in the array. The bulk substrate is  $250 \mu\text{m}$  with  $10\text{-}\Omega \cdot \text{cm}$  resistivity. The substrate is not thinned and no silicon lens is used for surface wave correction.

The near-field sensing method allows us to optimally place the radiator cores unconstrained by the coupling network. The DARs are separated by nearly  $600 \mu\text{m}$ , which approximately corresponds to the optimal spacing for the dominant surface mode at 220 GHz to partially cancel. Each DAR is biased by

<sup>3</sup>The process supported circular inductors, which were modified into DARs. However, they can also be realized with octagonal resonators [25].

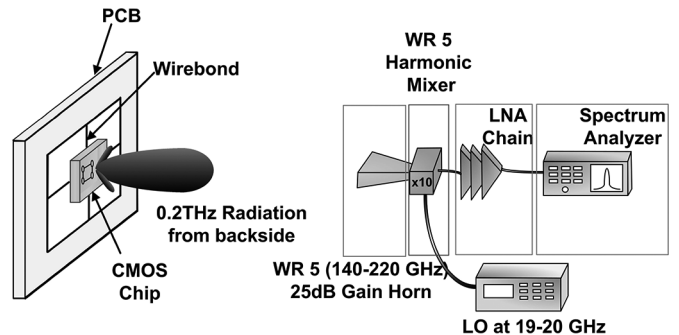


Fig. 13. Calibrated setup to measure frequency, EIRP, and radiation patterns of the second harmonic frequency near 200 GHz.

a network of t-lines in a grounded tub-shield, which provides open circuit impedances at both the frequency of oscillation  $f_0$  as well as the desired radiation frequency of  $2f_0$  [34].

The second harmonic signal radiated from the back of the substrate is captured with a WR-5 (140–220 GHz) 25-dB gain rectangular horn antenna, as shown in Fig. 13. The signal is then downconverted using a harmonic mixer, amplified by low-noise amplifiers, and then analyzed in a spectrum analyzer. The entire receiver chain is calibrated using a WR-5 source and Erickson power meter, which is a calorimeter-based power measurement instrument between 75–2000 GHz.

The effective isotropic radiated power (EIRP) in any given direction is measured directly from the power captured by the WR-5 receiver antenna at a far-field distance. The total radiated power, and hence, the directivity, is measured from the measured radiation pattern in space. It should be noted that, unlike passive antenna systems, we can only measure the directivity and not separately the gain of the radiating structure since the radiating second harmonic signals are generated internally in the DARs. The measured pattern gives us a measure of directivity.

Each DAR in the array has distributed varactor tuning to control resonance frequencies and phase of individual array element for the purpose of beam-steering. For nominal setting, the spectrum under locked condition is shown in Fig. 14. The signal is detected at a frequency of 191.2 GHz at a measured EIRP of  $-1.9 \text{ dBm}$ . The polarization of the signal is measured by rotating the receiver antenna and the received power remains almost constant, which illustrates that the radiated signal is nearly circularly polarized. The EIRP measurement is validated by measuring it over a range of far-field distances ( $R$ ) from 20 to 60 mm. Within the locking range, the varactor tuning introduces phase shifts in one or more of the radiators, which can be used for beam-scanning. When the coupled elements go outside the locking range, the spectrum splits, as also shown in Fig. 14.

Fig. 15 shows the measured radiation patterns. The patterns are rotationally symmetric due to the nature of the circularly polarized radiation from the symmetric  $2 \times 2$  array. Beam-scanning is demonstrated over two orthogonal planes by changing the varactor voltages of two adjacent DARs. The total electronic beam-scanning range is observed to be more than  $70^\circ$  in each of the two orthogonal axes. As shown in Section III, the steady-state phase difference ( $\phi_{f_0, \text{max}}$ ) between adjacent elements approaches  $90^\circ$  at the edge of the locking bandwidth. In practice, due to mismatches and loading effects of the bias network, the locking bandwidth is expected to decrease. Assuming  $\phi_{f_0, \text{max}} \approx 45^\circ$  ( $\phi_{2f_0} = 90^\circ$ ), we expect a total beam-scanning

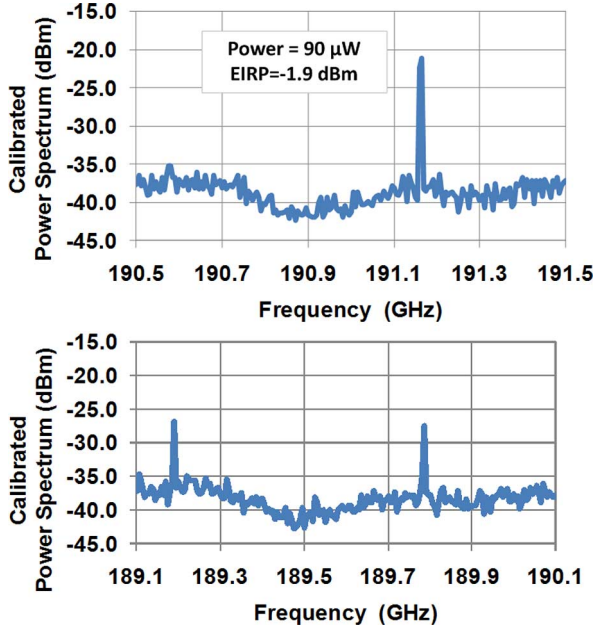


Fig. 14. Measured far-field spectrum of the radiated signal from the  $2 \times 2$  array (locked condition: upper figure, unlocked condition: lower figure).

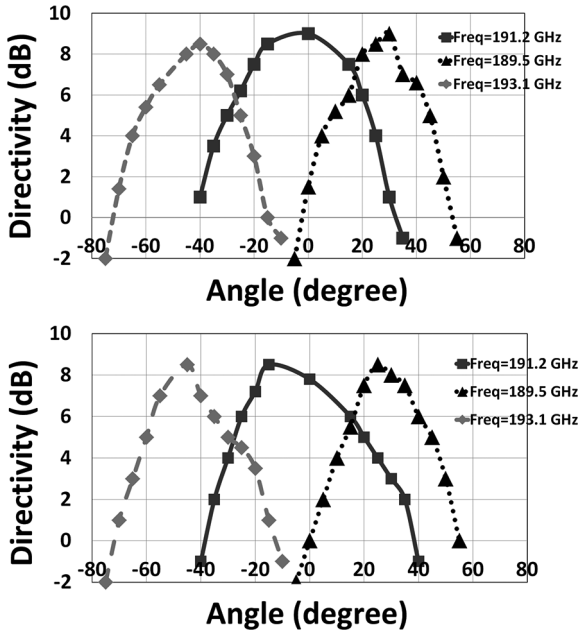


Fig. 15. Electronic beam-scanning near 190 GHz showing more than  $70^\circ$  variation in each of the two orthogonal axes.

range of  $2 \sin^{-1}(\lambda \Delta \phi_{2f_0} / (2\pi d_s)) \approx 82^\circ$  for on-chip separation of  $d_s = 600 \mu\text{m}$ . This is close to measurement results in Fig. 15. The frontside radiation pattern is also measured in the two orthogonal planes for nominal tuning, as shown in Fig. 16. The power radiated from the front side resulted in a total radiated power of  $90 \mu\text{W}$ , and a lower directivity of 8.5 dBi, compared to that reported in [34].

Fig. 17 shows the variation of the locked second harmonic frequency with control voltage. The measured locking bandwidth of 2 GHz at  $f_0$  is less than the estimated value in the analysis in Section III, possibly due to overestimation of the coupling strength. EIRP, measured from the backside of the chip over the beam-scanning range of over  $70^\circ$ , shows a fairly flat response

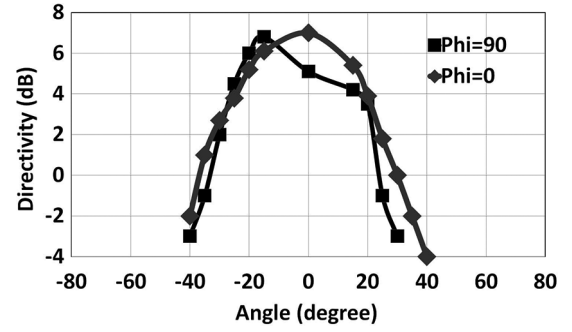


Fig. 16. Radiation patterns of the second harmonic power at 191.2 GHz from the front side of the  $2 \times 2$  array.

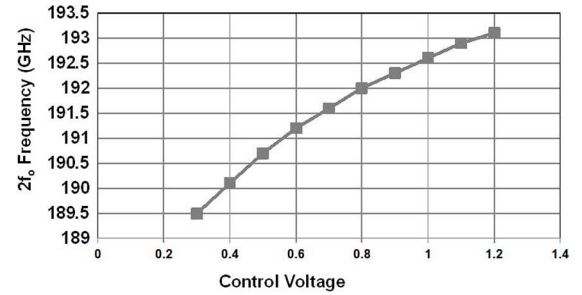


Fig. 17. Locked second harmonic frequency of the  $2 \times 2$  array when the varactor voltage of two adjacent DARs are varied simultaneously.

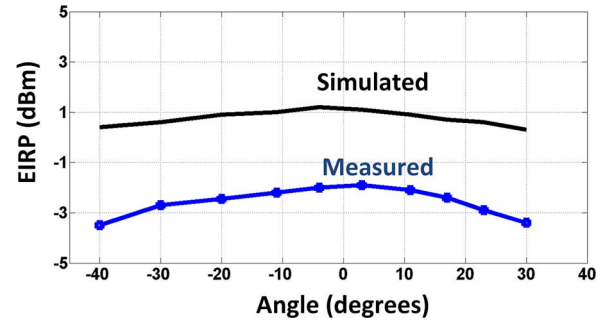


Fig. 18. EIRP variation over the beam-scanning range.

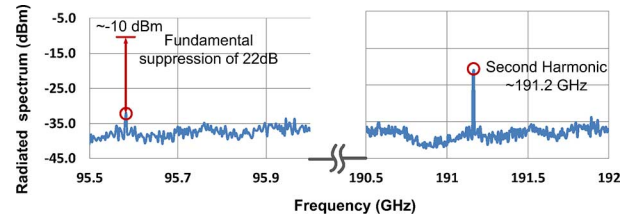


Fig. 19. Measurement of radiated fundamental power, which gets leaked out. The figure also shows the effective suppression of the undesired fundamental power by the DAR.

for a total variation of less than 1.6 dB, as shown in Fig. 18. The 3–4-dB difference between the simulated and measured EIRP, which is often observed at such high frequencies, could be the result of a combination of multiple factors such as lower harmonic generation near 200 GHz due to modeling inaccuracies in the circuit domain or due to lower radiation efficiency because of higher substrate losses in the antenna domain.

The DAR relies on the closely spaced out-of-phase currents to suppress radiation at the fundamental frequency. The measured spectrum of the fundamental and the second harmonic power is shown in Fig. 19. The spectrum at the fundamental frequency is

TABLE I  
SUMMARY OF SUB-MILLIMETER-WAVE RADIATING SOURCES

	Frequency (GHz)	Locking Mechanism	Antenna	Number of Elements	Beam-Scanning	EIRP (dBm)	DC Power (mW)	Silicon Technology
[24]	288	Single element (triple-push)	Diff. Ring with ext. lens	1	-	-	280	65-n m bulk CMOS
[26]	260	Central frequency is distributed and quadrupled	Leaky-wave	4	-	5	690	65-nm bulk CMOS
[27]	210	Fundamental frequency is distributed and radiated	Dipole	4	-	5.13	240	32-nm SOI CMOS
[28]	260	Mutually coupled through t-lines and doubled	Slot with ext. lens	8	-	15.7	800	65-nm bulk CMOS
[29]	170	Active doubler array	Slot with quartz superstrate	4	-	5	267	45-nm SOI CMOS
[30]	275-285	Central frequency reference locks arrays of DARs through t-lines	Traveling-wave	16	$\approx 80^\circ$ (2D)	9.4	810	45-nm SOI CMOS
[31]	161	Multi-phase oscillators driving multiple ports	Traveling-wave	1	-	4.6	388	130 nm SiGe
[32]	420	Active quadrupler array	Slot with quartz superstrate	8	-	3	700	45 nm SOI CMOS
[38]	338	Mutual coupling with t-lines	Patch	16	$\approx 45\text{-}50^\circ$	17.1	1540	65nm bulk CMOS
[39]	620	Coupled resonant tunneling diode osc.	Slot with offset feed	2	No	-2.1 (Rad Power)	-	GaInAs/AlAs
<b>This work</b>	<b>191</b>	<b>Near-field synch.</b>	<b>Traveling-wave radiator</b>	<b>4</b>	<b><math>\approx 70^\circ</math> (2D)</b>	<b>-1</b>	<b>77</b>	<b>65 nm bulk CMOS</b>

adjusted for the same receiver antenna aperture for a fair comparison of the radiation power density. The desired  $2f_0$  radiation power density at 191 GHz is shown to be 11 dB higher than that of the fundamental frequency at 95.5 GHz. The quasi-optical filtering suppresses the first harmonic by at least 22 dB internally in each DAR. The performance summary of sub-millimeter radiating sources, primarily in silicon, is presented in Table I. As can be seen, this work was the first demonstration of electronic-beam scanning in silicon at these frequencies and presents a scalable and robust method for synchronizing large-scale arrays in integrated technology.

## V. CONCLUSION

In this paper, near-field synchronization has been introduced as an efficient scalable robust method for beam-forming and beam-steering in large-scale arrays of radiating power sources in silicon at frequencies above  $f_{\max}$  of a technology. We demonstrate the proof-of-concept in an integrated  $2 \times 2$  CMOS array to show quasi-optical power combination and beam-steering near 200 GHz over  $70^\circ$  in both azimuth and elevation. The chip is realized in 65-nm bulk CMOS and occupies  $1 \text{ mm} \times 1.1 \text{ mm}$  in size.

### APPENDIX A

#### ON THE POSSIBILITY OF FALSE LOCKING

It is possible that two current configurations in a DAR result in the same sense antenna voltage, and therefore, can lead to false locking. However, it is seen that in integrated implementation, spurious substrate mode coupling is enough to suppress this undesired locking state. This is verified in simulations and experiments.

This is illustrated in Fig. 20. If we fix the direction of the traveling wave and the phase at any point on the DAR, then the current configuration for any other point on the DAR is fixed. If the phase of the oscillation is varied through  $360^\circ$ , it will be reflected *uniquely* in the sense antenna voltage. This will also be true if we reverse the wave direction. This implies that, for two

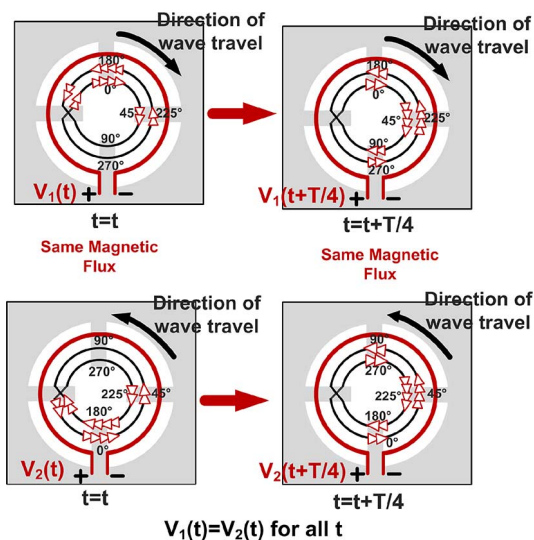


Fig. 20. Possibility of false locking and uniqueness of the sense antenna voltage as a measurement of the DAR state.

DARs, the sustaining wave travels in opposite directions, and there exist a state that results in the same sense antenna voltage. This is shown in Fig. 20, where the magnetic flux remains the same with time for the two states. If observed carefully, it can be seen that at all times, the current elements in one DAR are the rotational transformation of the elements in the other DAR, which results in the same magnetic flux. However, as discussed before, in practical realization, any form of coupling through substrate or otherwise, renders this state existing in two coupled DARs unstable.

### APPENDIX B

#### STABILITY ANALYSIS OF DISTRIBUTED NEAR-FIELD SYNCHRONIZATION

The stability analysis of the locked stated is based on the Stroboscopic concept [36]. While the detailed proof is beyond the scope of this paper [23], we highlight the key points. We assume

a locked frequency of  $\omega_0$  and observe the dynamics of the amplitudes and phases of the two coupled oscillators once every time period  $T = 2\pi/\omega_0$ . Thereby, we observe a discrete set of points in the amplitude and phase space  $(r_{1,T}, \phi_{1,T}, r_{2,T}, \phi_{2,T})$  evolving with time. These become the state variables and we analyze the stability of the steady-state solutions in this new formed phase space [36]. If the coupled system reaches a stable-steady oscillatory state with common frequency  $\omega_0$ , the amplitude and phase observed every time period  $T$  will remain the same, and any perturbation will bring back the system into this steady-state solution in the new phase space.

By transforming the second-order system in (3) into two first-order equations in the state space variables  $r$  and  $\phi$ , where  $v = r \cos(\phi)$  and  $(dv)/(dt) = \omega_0 r \sin(\phi)$  and integrating over one time period  $T$ , we obtain the state differential equations in the discrete time space as

$$\frac{dr_{1,T}}{dt_T} \approx -\frac{\omega_{t,1}}{2Q} r_{1,T} \left(1 - g_m R + \frac{3}{4} \alpha_3^2 R r_{1,T}^2\right) + \frac{C\omega_0}{2} (r_{2,T} \cos(\phi_{2,T} - \phi_{1,T}) - r_{1,T}) \quad (7a)$$

$$\frac{d\phi_{1,T}}{dt_T} = \frac{\Delta\omega_t}{2} + \frac{C\omega_0}{2} \frac{r_{2,T}}{r_{1,T}} \sin(\phi_{2,T} - \phi_{1,T}) \quad (7b)$$

$$\frac{dr_{2,T}}{dt_T} \approx -\frac{\omega_{t,2}}{2Q} r_{2,T} \left(1 - g_m R + \frac{3}{4} \alpha_3^2 R r_{2,T}^2\right) + \frac{C\omega_0}{2} (r_{1,T} \cos(\phi_{2,T} - \phi_{1,T}) - r_{2,T}) \quad (7c)$$

$$\frac{d\phi_{2,T}}{dt_T} = -\frac{\Delta\omega_t}{2} + \frac{C\omega_0}{2} \frac{r_{1,T}}{r_{2,T}} \sin(\phi_{1,T} - \phi_{2,T}). \quad (7d)$$

From (7a)–(7d), we obtain the steady-state amplitude as  $r_{1,T}^0 \approx r_{2,T}^0 = \sqrt{4(g_m R - 1)/(3\alpha_3^2 R)}$  and phase as  $\sin(\phi_{1,T}^0 - \phi_{2,T}^0) = \Delta\omega_t/(C\omega_0)$ . We obtained the same results in the steady-state analysis in (5). The stability of this steady-state solution can be investigated by linearizing the dynamical equations (7a)–(7d) around the equilibrium point. The state-space matrix  $A$  is given by

$$A = \begin{pmatrix} -\beta & -r_T^0 \frac{\Delta\omega_t}{2} & \gamma & r_T^0 \frac{\Delta\omega_t}{2} \\ \frac{\Delta\omega_t}{2r_T^0} & -\gamma & -\frac{\Delta\omega_t}{2r_T^0} & \gamma \\ \gamma & -r_T^0 \frac{\Delta\omega_t}{2} & -\beta & r_T^0 \frac{\Delta\omega_t}{2} \\ \frac{\Delta\omega_t}{2r_T^0} & \gamma & -\frac{\Delta\omega_t}{2r_T^0} & -\gamma \end{pmatrix} \quad (8)$$

where the steady-state value  $r_T^0 = r_{1,T}^0 \approx r_{2,T}^0 = \sqrt{4(g_m R - 1)/(3\alpha_3^2 R)}$ ,  $\Delta\phi_T^0 = \Delta\phi_{1,T}^0 - \Delta\phi_{2,T}^0$ ,  $\beta \approx (\omega_0)/(Q)(g_m R - 1) + (C\omega_0)/(2)$ , and  $\gamma = (C\omega_0)/(2) \cos(\Delta\phi_T^0)$ .

It is trivial to prove that the determinant of the matrix  $A$  is 0, which implies one eigenvalue  $\lambda_1 = 0$ . It can be shown that the other eigenvalues are  $\lambda_2 = -2\gamma < 0$ ,  $\lambda_3 = -(\gamma + \beta) < 0$ , and  $\lambda_4 = -(\beta - \gamma) < 0$ . Solving for the eigenvectors, it is easy to show that any perturbation in state space variables dies down as

$$\delta r_{1,T}/\delta r_{2,T} = C_1 e^{\lambda_2 t} + C_2 e^{\lambda_3 t} + C_3 e^{\lambda_4 t} \quad (9a)$$

$$\delta(\phi_{1,T} - \phi_{2,T}) = C_4 e^{\lambda_2 t} + C_5 e^{\lambda_3 t} \quad (9b)$$

where  $\lambda_2, \lambda_3, \lambda_4 < 0$ . Since the initial phase is arbitrary, we only consider perturbation in the difference of the phase variables of the two DARs (i.e.,  $\delta(\phi_{1,T} - \phi_{2,T})$ ), which is shown to

exponentially decay to zero. This implies, that the steady-state solution that exists within the locking range is stable. The analysis can be extended to larger arrays of mutually coupled traveling-wave oscillators where the derived stability conclusions still hold.

#### ACKNOWLEDGMENT

The authors would like to thank Prof. J. Zmuidzinas, Prof. G. Blake, D. Miller, Dr. P. Siegel, Prof. D. Rutledge, and Dr. Sandy Weinreb for technical discussions and providing some of the measurement equipments.

#### REFERENCES

- [1] M. Tonouchi, "Cutting-edge terahertz technology," *Nature Photon.*, vol. 1, pp. 97–105, 2007.
- [2] P. H. Siegel, "Terahertz technology," *IEEE Trans. Microw. Theory Techn.*, vol. 50, no. 3, pp. 910–928, Mar. 2002.
- [3] K. B. Cooper, R. J. Dengler, N. Llombart, B. Thomas, G. Chattopadhyay, and P. H. Siegel, "THz imaging radar for standoff personnel screening," *IEEE Trans. THz Sci. Technol.*, vol. 1, no. 1, pp. 169–182, Sep. 2011.
- [4] L. A. Samoska, "An overview of solid-state integrated circuit amplifiers in the submillimeter-wave and THz regime," *IEEE Trans. THz Sci. Technol.*, vol. 9, no. 1, pp. 9–24, Sep. 2011.
- [5] H.-J. Song, J.-Y. Kim, K. Ajito, M. Yaita, and N. Kukutsu, "Fully integrated ASK receiver MMIC for terahertz communications at 300 GHz," *IEEE Trans. THz Sci. Technol.*, vol. 3, no. 4, pp. 445–452, Jul. 2013.
- [6] J. Hacker, M. Urteaga, M. Seo, A. Skalare, and R. Lin, "InP HBT amplifier MMICs operating to 0.67 THz," in *IEEE MTT-S Int. Microw. Symp. Dig.*, Jun. 2013.
- [7] O. Momeni and E. Afshari, "Higher power terahertz and millimeter-wave oscillator design: A systematic approach," *IEEE J. Solid-State Circuits*, vol. 46, no. 3, pp. 583–597, Mar. 2011.
- [8] Y. Tousi, O. Momeni, and E. Afshari, "A 283–296 GHz VCO with 0.76 mW output power in 65 nm CMOS," in *IEEE Int. Solid-State Circuits Conf. Tech. Dig.*, Feb. 2012, pp. 258–260.
- [9] D. Shim, D. Koukis, D. J. Arenas, D. B. Tanner, and K. O. Kenneth, "553 GHz signal generation in CMOS using quadrature-push oscillator," in *VLSI Circuits Symp. Dig.*, Jun. 2011, pp. 154–155.
- [10] J. Sharma and H. Krishnaswamy, "216- and 316-GHz 45-nm SOI CMOS signal sources based on a maximum-gain ring oscillator topology," *IEEE Trans. Microw. Theory Techn.*, vol. 61, no. 1, pp. 492–504, Jan. 2013.
- [11] D. Huang *et al.*, "324 GHz CMOS frequency generator using linear superposition technique," in *IEEE Int. Solid-State Circuits Conf. Tech. Dig.*, Feb. 2008, pp. 476–477.
- [12] E. Seok *et al.*, "A 410 GHz CMOS push-push oscillator with an on-chip patch antenna," in *IEEE Int. Solid-State Circuits Conf. Tech. Dig.*, Feb. 2008, pp. 472–473.
- [13] D. B. Rutledge, D. P. Neikirk, and D. P. Kasilingam, "Integrated-circuit antennas," in *Infrared and Millimeter-Waves*. New York, NY, USA: Academic, 1983, pp. 1–90.
- [14] D. F. Filipovic, G. P. Gauthier, S. Raman, and G. M. Rebeiz, "Off axis properties of silicon and quartz dielectric lens antennas," *IEEE Trans. Antennas Propag.*, vol. 45, no. 5, pp. 760–766, May 1997.
- [15] R. A. York and R. C. Compton, "Quasi-optical power combining using mutually synchronized oscillator array," *IEEE Trans. Microw. Theory Techn.*, vol. 39, no. 6, pp. 1000–1009, Jun. 1991.
- [16] P. Liao and R. A. York, "A new phase-shifterless beam-scanning technique using array of coupled oscillators," *IEEE Trans. Microw. Theory Techn.*, vol. 41, no. 10, pp. 1810–1815, Oct. 1993.
- [17] R. A. York and Z. B. Popovic, *Active and Quasi-Optical Arrays for Solid-State Power Combining*. New York, NY, USA: Wiley, 1997.
- [18] J. Hwang and N. Myung, "A new beam-scanning technique by controlling the coupling angle in a coupled oscillator array," *IEEE Microw. Guided Wave Lett.*, vol. 8, no. 5, pp. 191–193, May 1998.
- [19] R. York and R. Compton, "Measurement and modelling of radiative coupling in oscillator arrays," *IEEE Trans. Microw. Theory Techn.*, vol. 41, no. 10, pp. 438–444, Mar. 1993.
- [20] D. B. Rutledge, N.-S. Cheng, R. A. York, R. M. Weikle, II, and M. P. De Liso, "Failures in power-combining arrays," *IEEE Trans. Microw. Theory Techn.*, vol. 47, no. 7, pp. 1077–1082, Jul. 1999.
- [21] Z. B. Popović and D. B. Rutledge, "Diode-grid oscillators," in *Proc. IEEE AP-S Int. Symp.*, 1988, pp. 442–445.

- [22] Z. B. Popović, R. M. Weikle, M. Kim, K. A. Potter, and D. B. Rutledge, "Bar-grid oscillators," *IEEE Trans. Microw. Theory Techn.*, vol. 38, no. 3, pp. 225–230, Mar. 1990.
- [23] K. Sengupta, "Silicon-based terahertz circuits and systems," Ph.D. dissertation, Elect. Eng. Dept., California Inst. Technol., Pasadena, CA, USA, 2012.
- [24] Y. Zhao, J. Grzyb, and U. R. Pfeiffer, "A 288-GHz lens-integrated balanced triple-push source in a 65-nm CMOS technology," in *Eur. Solid-State Circuits Conf.*, Bordeaux, France, Sep. 2012, pp. 289–292.
- [25] K. Sengupta and A. Hajimiri, "Distributed active radiator for THz signal generation," in *IEEE Int. Solid-State Circuits Conf. Tech. Dig.*, Feb. 2011, pp. 288–289.
- [26] J. Park, S. Kang, S. Thyagarajan, E. Alon, and A. M. Niknejad, "A 260 GHz fully integrated CMOS transceiver for wireless chip-to-chip communication," in *VLSI Circuits Symp. Dig.*, Jun. 2012, pp. 48–49.
- [27] Z. Wang, P. Chiang, P. Nazari, C. Wang, Z. Chen, and P. Heydari, "A 210 GHz fully integrated differential transceiver with fundamental-frequency VCO in 32 nm SOI CMOS," in *IEEE Int. Solid-State Circuits Conf. Tech. Dig.*, Feb. 2013, pp. 136–137.
- [28] R. Han and E. Afshari, "A 260 GHz broadband source with 1.1 mW continuous-wave radiated power and EIRP of 15.7 dBm in 65 nm CMOS," in *IEEE Int. Solid-State Circuits Conf. Tech. Dig.*, Feb. 2013, pp. 138–139.
- [29] F. Goleuk, J. M. Edwards, B. Cetinoneri, Y. A. Atesal, and G. M. Rebeiz, "A 163–180 GHz  $2 \times 2$  amplifier-doubler array with peak EIRP of +5 dBm," in *IEEE RFIC Symp. Dig.*, Jun. 2013, pp. 363–366.
- [30] K. Sengupta and A. Hajimiri, "0.28 THz  $4 \times 4$  power-generation and beam-steering array," in *IEEE Int. Solid-State Circuits Conf. Tech. Dig.*, Feb. 2012, pp. 256–257.
- [31] S. M. Bowers and A. Hajimiri, "Multi-port driven radiators," *IEEE Trans. Microw. Theory Techn.*, vol. 61, no. 12, pp. 4428–4441, Dec. 2013.
- [32] F. Goleuk, D. O. Gurbuz, and G. M. Rebeiz, "A 0.39–0.44 THz  $2 \times 4$  amplifier-quadrupler array with peak EIRP of 3–4 dBm," *IEEE Trans. Microw. Theory Techn.*, vol. 61, no. 12, pp. 4483–4491, Dec. 2013.
- [33] K. Sengupta and A. Hajimiri, "0.28 THz power-generation and beam-steering array in CMOS based on distributed active radiators," *IEEE J. Solid-State Circuits*, vol. 47, no. 12, pp. 3013–3031, Dec. 2012.
- [34] K. Sengupta and A. Hajimiri, "Sub-THz beam-forming using near-field coupling of distributed active radiator arrays," in *IEEE RFIC Symp. Dig.*, Jun. 2011, pp. 357–360.
- [35] A. Pivovsky, M. Rosenblum, and J. Kurths, *Synchronization: A Universal Concept in Nonlinear Sciences*. Cambridge, U.K.: Cambridge Univ. Press, 2003.
- [36] K. Sengupta, T. K. Bhattacharyya, and H. Hashemi, "A nonlinear transient analysis of regenerative frequency dividers," *IEEE Trans. Circuits Syst. I, Reg. Papers*, vol. 54, no. 12, pp. 2646–2660, Dec. 2007.
- [37] J. A. Hagerty and Z. Popovic, "A 10 GHz integrated class-E oscillating annular ring element for high-efficiency transmitting arrays," in *IEEE MTT-S Int. Microw. Symp. Dig.*, Jun. 2002, vol. 2, pp. 1317–1320.
- [38] Y. Touse and E. Afshari, "A scalable THz 2D phased array with +17 dBm of EIRP at 338 GHz in 65 nm bulk CMOS," in *IEEE Int. Solid-State Circuits Conf. Tech. Dig.*, Feb. 2014, pp. 258–259.
- [39] S. Suzuki, M. Shiraiishi, H. Shibayama, and M. Asada, "High-power operation of terahertz oscillators with resonant tunneling diodes using impedance-matched antennas and array configuration," *IEEE J. Sel. Topics Quantum Electron.*, vol. 19, no. 1, Jan./Feb. 2013.



**Kaushik Sengupta** (M'12) received the B.Tech. and M.Tech. degrees in electronics and electrical communication engineering from the Indian Institute of Technology (IIT), Kharagpur, India, both in 2007, and the M.S. and Ph.D. degrees in electrical engineering from the California Institute of Technology, Pasadena, CA, USA, in 2008 and 2012, respectively.

In February 2013, he joined the faculty of the Department of Electrical Engineering, Princeton University, Princeton, NJ, USA. During his undergraduate studies, in the summers of 2005 and 2006, he performed research at the University of Southern California and the Massachusetts Institute of Technology (MIT), where he was involved with nonlinear integrated systems for high-purity signal generation and low-power RF iden-

tification (RFID) tags, respectively. His research interests are in the areas of high-frequency integrated circuits (ICs), electromagnetics, optics for various applications in sensing, imaging, and high-speed communication.

Dr. Sengupta was the recipient of the IBM Ph.D. fellowship (2011–2012), the IEEE Solid-State Circuits Society Predoctoral Achievement Award (2012), the IEEE Microwave Theory and Techniques Graduate Fellowship (2012), and the Analog Devices Outstanding Student Designer Award (2011). He was the recipient of the Charles Wilts Prize in 2013 from Electrical Engineering, Caltech for outstanding independent research in electrical engineering leading to a Ph.D. He was also the recipient of the Prime Minister Gold Medal Award of IIT (2007), the Caltech Institute Fellowship, the Most Innovative Student Project Award of the Indian National Academy of Engineering (2007), and the IEEE Microwave Theory and Techniques Undergraduate Fellowship (2006). He serves on the Technical Program Committee of the European Solid-State Circuits Conference (ESSCIRC). He was selected in "Princeton Engineering Commendation List for Outstanding Teaching" in 2014. He was the corecipient of the IEEE RFIC Symposium Best Student Paper Award in 2012 and 2015 IEEE Microwave Theory and Techniques Society (IEEE MTT-S) Microwave Prize.



**Ali Hajimiri** (F'10) received the B.S. degree in electronics engineering from the Sharif University of Technology, Tehran, Iran, in 1994, and the M.S. and Ph.D. degrees in electrical engineering from Stanford University, Stanford, CA, USA, in 1996 and 1998, respectively.

From 1993 to 1994, he was a Design Engineer with Philips Semiconductors, where he was involved with a BiCMOS chipset for global system for mobile communication (GSM) and cellular units. In 1995, he was with Sun Microsystems, where he was involved with

the UltraSPARC microprocessors cacheRAM design methodology. During the summer of 1997, he was with Lucent Technologies (Bell Laboratories), Murray Hill, NJ, USA, where he investigated low-phase-noise integrated oscillators. In 1998, he joined the faculty of the California Institute of Technology, Pasadena, CA, USA, where he is currently the Thomas G. Myers Professor of Electrical Engineering and the Director of the Microelectronics Laboratory. In 2002, he cofounded Axiom Microdevices Inc., whose fully integrated CMOS power amplifier (PA) has shipped close to 200 million units, and was acquired by Skyworks Inc. in 2009. He has authored or coauthored over 150 refereed journal and conference technical papers. He authored *The Design of Low Noise Oscillators* (Springer, 1999). He was a Guest Editorial Board member of the *Transactions of the Institute of Electronics, Information and Communication Engineers*, Japan. He holds over 60 U.S. and European patents. His research interests are high-speed and high-frequency integrated circuits (ICs) for applications in sensors, biomedical devices, photonics, and communication systems.

Dr. Hajimiri has served on the Technical Program Committee (TPC), International Solid-State Circuits Conference (ISSCC). He has served as an associate editor for the IEEE JOURNAL OF SOLID-STATE CIRCUITS and the IEEE TRANSACTIONS ON CIRCUITS AND SYSTEMS—II: EXPRESS BRIEFS. He is a member of the TPCs of the International Conference on Computer-Aided Design (ICCAD). He was a guest editor of the IEEE TRANSACTIONS ON MICROWAVE THEORY AND TECHNIQUES. He has served on the Guest Editorial Board of the TRANSACTIONS OF THE INSTITUTE OF ELECTRONICS, INFORMATION AND COMMUNICATION ENGINEERS (IEICE), Japan. He was selected to the TR35 Top Innovators List (formerly the TR100) in 2004. He has served as a Distinguished Lecturer of the IEEE Solid-State Circuits Society and the IEEE Microwave Theory and Techniques Society (IEEE MTT-S). He was the recipient of the California Institute of Technology Graduate Students Council Teaching and Mentoring Award, as well as the Associated Students of the California Institute of Technology Undergraduate Excellence in Teaching Award. He was the Gold Medal recipient of the National Physics Competition and the Bronze Medal recipient of the 21st International Physics Olympiad, Groningen, The Netherlands. He was a corecipient of the IEEE JOURNAL OF SOLID-STATE CIRCUITS Best Paper Award of 2004 and the International Solid-State Circuits Conference (ISSCC) Jack Kilby Outstanding Paper Award. He was a two-time corecipient of the CICC's Best Paper Award and a three-time recipient of the IBM Faculty Partnership Award, as well as the National Science Foundation CAREER Award and Okawa Foundation Award. He was a recipient of the 2015 IEEE MTT-S Microwave Prize.